KeAi

CHINESE ROOTS
GLOBAL IMPACT

Contents lists available at ScienceDirect

Petroleum Science

journal homepage: www.keaipublishing.com/en/journals/petroleum-science



Original Paper

Evaluation of the combined influence of geological layer property and in-situ stresses on fracture height growth for layered formations



Peng Tan ^{a, b}, Zhao-Wei Chen ^{a, b}, Liu-Ke Huang ^{c, *}, Qing Zhao ^{a, b}, Sha-Rui Shao ^d

- ^a CNPC Engineering Technology R&D Company Limited, Beijing, 102206, China
- ^b National Engineering Research Center for Oil & Gas Drilling and Completion Technology, Beijing, 102206, China
- ^c School of Civil Engineering and Geomatics, Southwest Petroleum University, Chengdu, 610500, Sichuan, China
- ^d Shale Gas Research Institute, Southwest Oil & Gas Field Company, Chengdu, 610051, Sichuan, China

ARTICLE INFO

Article history: Received 22 December 2023 Received in revised form 8 July 2024 Accepted 13 July 2024 Available online 14 July 2024

Edited by Yan-Hua Sun

Keywords:
Deep shale
Hydraulic fracturing
HF propagation
Fracture interaction
Cohesive zone method

ABSTRACT

Fracture geometry is important when stimulating low-permeability reservoirs for natural gas or oil production. The geological layer (GL) properties and contrasts in in-situ stress are the two most important parameters for determination of the vertical fracture growth extent and containment in layered rocks. However, the method for assessing the cumulative impact on growth in height remains ambiguous. In this research, a 3D model based on the cohesive zone method is used to simulate the evolution of hydraulic fracture (HF) height in layered reservoirs. The model incorporates fluid flow and elastic deformation, considering the friction between the contacting fracture surfaces and the interaction between fracture components. First, an analytical solution that was readily available was used to validate the model. Afterwards, a quantitative analysis was performed on the combined impacts of the layer interface strength, coefficient of interlayer stress difference, and coefficient of vertical stress difference. The results indicate that the observed fracture height geometries can be categorized into three distinct regions within the parametric space: blunted fracture, crossed fracture, and T-shaped fracture. Furthermore, the results explained the formation mechanism of the low fracture height in the deep shale reservoir of the Sichuan Basin, China, as well as the distinction between fracture network patterns in mid-depth and deep shale reservoirs.

© 2024 The Authors. Publishing services by Elsevier B.V. on behalf of KeAi Communications Co. Ltd. This is an open access article under the CC BY-NC-ND license (http://creativecommons.org/licenses/by-nc-nd/4.0/).

4.0//

1. Introduction

A key task in the massive hydraulic fracturing process was predicting the geometry and properties of hydraulically produced fractures. Early models, which were primarily two-dimensional or radial, lacked consideration for height growth through layered rock systems, resulting in a simplified representation of fractures (Perkins and Kern, 1961; Geertsma and De Klerk, 1969; Nordgren, 1972). In contrast to fracture shapes observed in homogeneous single lithologic reservoirs, hydraulic fracture (HF) in layered formations is considerably more complex due to the influence of multiple factors such as in-situ stress, interlayer lithology, and interface conditions (Li et al., 2020; Luo et al., 2022; Yan et al., 2019, 2021; Zhang et al., 2022; Huang et al., 2023a; Zou et al., 2016a). At

* Corresponding author.

E-mail address: swpuhlk@126.com (L.-K. Huang).

this time, it is unclear how to accurately predict the growth of HFs in layered formations.

In an effort to establish methods for predicting the growth of HF in layered formation, numerous studies have been conducted. In terms of theoretical models, Simonson et al. (1979) established a mathematical model of layered media based on linear elastic fracture mechanics. It turned out that the stress factor in the fracture tip was tending to be positive infinity when HF growth from low modulus to high modulus was predicted to be suppressed. However, van Eekelen (1982), Ahmed (1984), and Fung et al. (1987) argued that the vital factor of fracture height was the stress difference between layers, and the modulus difference was not critical for the fracture penetration into layers. Smith et al. (2001) studied how the modulus difference between layers influenced fracture propagation by influencing the fracture width and fluid pressure in fracture, which influenced the fracture height in an indirect way. Chuprakov and Prioul (2015) established 2D numerical models containing T-shape fractures to study the influence of interface

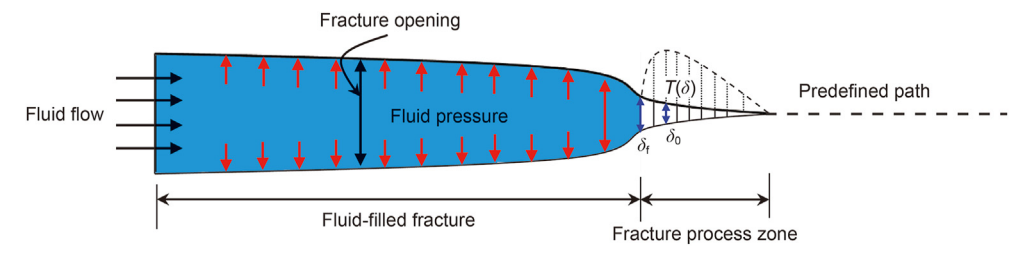


Fig. 1. Predefined cohesive zone demonstration for either HF or GL (Chen et al., 2017).

properties on fracture propagation in the vertical direction and predicted slippage displacement of the fracture tip as well as an increase in the volume of fracture. And critical conditions and critical pressure for fracture penetration into the interface were given. Later, Guo et al. (2018) and Zheng et al. (2022) created a model for a T-shape fracture and used a pressure drop model to study the three-dimensional shape of HF propagation. Oyedokun and Schubert (2017) established a mathematical model for multilayer anisotropic layered media using the energy conservation method and proposed the concept of effective fracture toughness. Zhang and Jeffrey (2008) and Yan and Yu (2022) studied an HF crossing a natural fracture and included full coupling in 2D with friction. Huang and Liu (2018) established a three-dimensional model considering the effects of longitudinal fluid flow, fluid filtration, and bedding and obtained the criterion for HF penetration through bedding. Fu et al. (2018) and Xing et al. (2017) established an analytical model for the vertical propagation of HF and studied the effect of interface properties and in-situ stress on the vertical propagation of HF.

In terms of physical simulation, Warpinski et al. (1982) and Teufel and Clark (1984) have shown that the interfacial shear strength and the minimum horizontal stress difference between layers were the most critical parameters for controlling fracture propagation. When the in-situ stress difference between layers was 2–3 MPa, it was enough to prevent the HF from extending in the height direction. Jeffrey and Bunger (2007) used PMMA transparent material to carry out true triaxial laboratory experiments and studied the vertical propagation characteristic of HFs under different interlayer stress conditions. Xing et al. (2018a) summarized four fracture patterns. Goldstein and Osipenko (2015) studied the effect of interfacial friction characteristics on the propagation pattern of dry fractures. It was found that the interface slipped when the fractures extended into the frictional interface, and the larger the inclination angle of the interface, the larger the slip distance. Fu et al. (2016) also observed a similar phenomenon by conducting laboratory true triaxial hydraulic fracturing experiments. Tan et al. (2023) carried out hydraulic fracturing physical simulation experiments in coal-measure strata and found that the vertical expansion of HFs tended to show the characteristic of asymmetric expansion. Aiming at the fracture height growth behavior of layered shale reservoirs, Hou et al. (2019), Zhang et al. (2019), Huang et al. (2022, 2024) and Li et al. (2018) have found that the bedding plane has a significant influence on the process of fracture height growth through laboratory experiments. By analyzing a large number of hydraulic fracturing experiments, Tan et al. (2017) summarized and obtained four typical HF geometry types in vertical direction: simple transverse fracture, fishbone-like fracture, fishbone-like fracture connecting natural fracture (NF), and multilateral fishbone-like fracture network.

In terms of numerical simulation, Huang et al. (2019, 2020, 2023b), Zhang et al. (2017, 2019, 2020), Zhou et al. (2016), He et al. (2023) and Wang et al. (2017) used the discrete element method to establish the fluid—solid coupling model of multi-layer fracturing.

The study showed that the vertical heterogeneity of layered rock seriously affected the extension path of HF. Xing et al. (2018b) used the lattice method to simulate the interaction mechanism between HF and GL, Zou et al. (2016a) established a HF propagation model of a three-dimensional layered stratum by a numerical method combining finite elements and discrete elements and studied the effects of anisotropy and construction parameters on the threedimensional extension of HF and injection pressure. Tang and Wu (2018) studied the penetration behavior of HF in multilayer media using the three-dimensional displacement discontinuity method. Zhu et al. (2015) and Li Y. et al. (2017) used the cohesive zone method to establish a hydraulic fracturing model for layered sandstone reservoirs and studied how the difference in in-situ stress and physical properties between layers influenced the fracture shape and the size of fractures under fluid-solid coupling conditions. However, the GL in their model was assumed to be well cemented. Using the same numerical method. Chen et al. (2017) and Haddad (2017) studied the interaction mechanism between HF and NF. At the same time, Guo et al. (2017) used the typical shale gas well in the field as an example to simulate the 2D interaction mechanism between HF and GL and analyzed the influence of geological and engineering parameters on the fracture propagation law and the fracture width. Ouchi et al. (2017) established a peridynamics-based hydrodynamic fracturing model, studied the propagation behavior of HFs in a vertical direction, and obtained three types of HFs: penetration, kinking, and bifurcation. The results were consistent with the experimental results of Altammar et al. (2019).

The GL was a unique structure for the layered formations. When the HF extended to weakly cemented surfaces, the fracture geometry and the pressure inside the fracture could change significantly, which had an important influence on the height propagation behavior. In the above studies, physical simulation studies (Tan et al., 2017; Zou et al., 2016b; Zhang et al., 2019; Han et al., 2024) were mostly qualitative and lacked quantitative characterization. The fracture height prediction model (Fung et al., 1987; Zhao et al.,

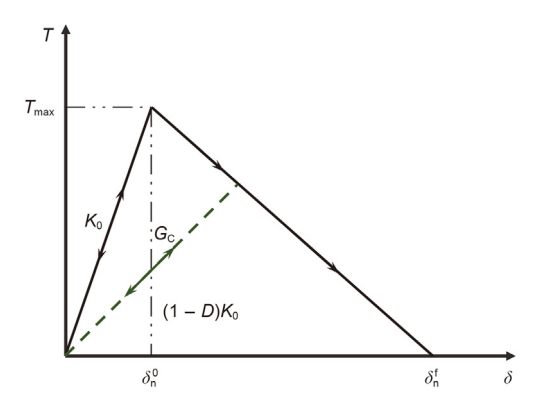


Fig. 2. Bilinear cohesive traction separation law.

2013) assumed that the GL was well cemented or ignored the interface frictional slippage. At the same time, since the HF extension was a three-dimensional expansion process, the fracture length and the fracture height changed simultaneously. At present, two-dimensional models for studying fracture height growth are dominant (Gu et al., 2012; Zhao and Chen, 2010; Liu and Valko, 2015), which ignored changes in the length of the fracture, result in high fracture height prediction results, and cannot effectively guided the optimal fracturing design. Therefore, a need exists to study the intersection mechanism of HF and GL in three-dimensional space and to explore the fracture propagation behavior under simultaneous changes in fracture height and fracture length.

In this paper, a three-dimensional HF propagation numerical model that includes interface friction characteristics was established based on the cohesive zone finite element method. The competitive propagation behavior of HFs in the length, width, and height direction was studied. The influences of interface strength and in-situ stress on the intersection of HF and GL were quantitatively characterized, and a controlling chart was formed to grasp the mechanism of HF initiation and vertical penetration in layered reservoirs. Finally, the results of this paper provided a scientific explanation for the formation mechanism of fracture geometry of deep and mid-depth shale reservoirs in the Sichuan Basin, China.

2. Basic theory

In this study, a 3D model using the cohesive zone method was established to study the height growth behavior of HF encountering GL. This model combines several physical processes: (1) fracture propagation, (2) fluid flow within the fractures, and (3) rock deformation near fractures. A cohesive pore pressure element was used to simulate fluid flow and 3D fracture propagation. Based on this model, the interaction of HF and GL, as well as their morphologies, could be modeled.

Both HF and GL were simulated by the cohesive zone finite element. The cohesive zone model requires pre-defining the fracture surface of HF and GL, which consist of cohesive parts that adhere to the traction-separation behavior. The HF would extend along this pre-defined path during the simulation stage, as shown in Fig. 1 (Chen et al., 2017). Initially, the cohesive fracture is unbroken and closed. With the injection of fracturing fluids, the cohesive element is pressurized, and the traction increases. The cohesive fracture tip began to be damaged as the traction on the fracture surface reached the cohesive strength $T_{\rm max}$ and the separation reached the critical value δ_0 (see Fig. 2). And then material

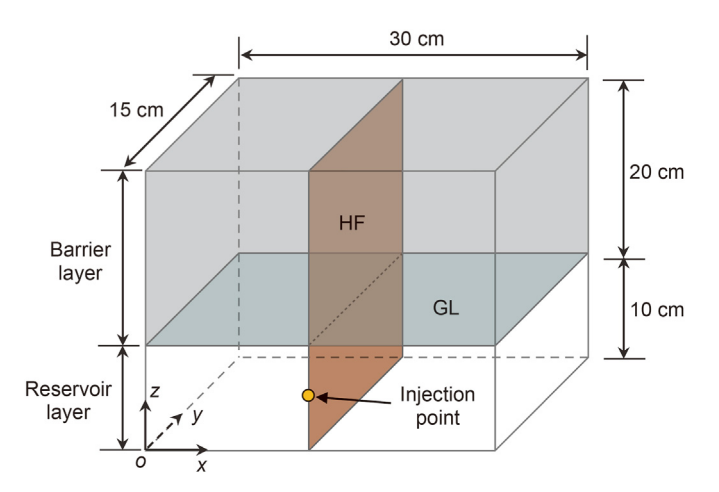


Fig. 3. Illustrations of the HF and GL intersection model.

Table 1 Input parameters for benchmark case.

Parameter	Value
Young's modulus E, GPa	5
Poisson's ratio v	0.25
Vertical stress σ_V , MPa	5
Maximum principle horizontal stress σ_{H} , MPa	3
Minimum principle horizontal stress σ_h , MPa	1
Injection rate Q, m ³ /s	10^{-6}
Fluid viscosity μ , Pa·s	0.3
Tensile strength T, MPa	0.5

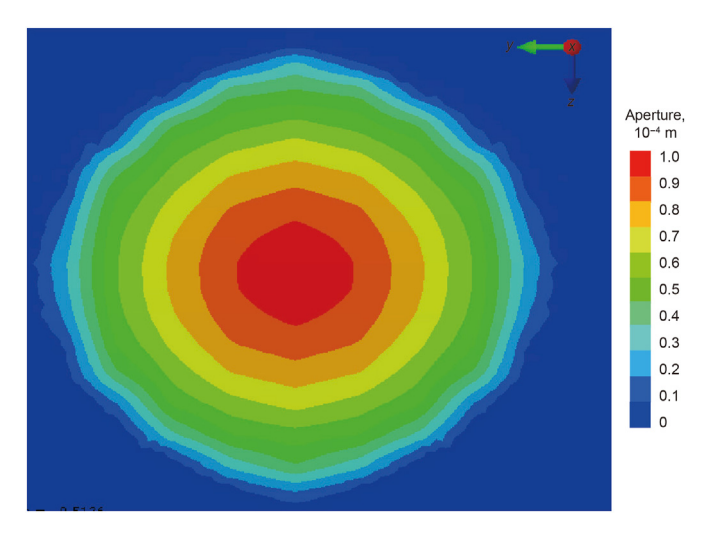


Fig. 4. Aperture of HF in the verification case.

degradation occurs until the material fracture tip fails completely as the traction and separation reached zero and critical value $\delta_{\rm f}$, respectively. After the cohesive element is broken, fracturing fluids enter the damaged zone.

2.1. The cohesive law

In this paper, a bilinear cohesive traction-separation law was used in the model, as illustrated in Fig. 2. The quadratic interaction function involving the nominal stress ratios equaled 1 when the damage was about to happen, which could be expressed as (Abaqus, 2014)

$$\left\{ \frac{\langle \sigma_{n} \rangle}{\sigma_{n}^{\text{max}}} \right\}^{2} + \left\{ \frac{\tau_{s}}{\tau_{s}^{\text{max}}} \right\}^{2} \left\{ \frac{\tau_{t}}{\tau_{t}^{\text{max}}} \right\}^{2} = 1$$
(1)

where $\sigma_{\rm n}^{\rm max}$, $\tau_{\rm s}^{\rm max}$, and $\tau_{\rm t}^{\rm max}$ are the peak values of the nominal stress when the deformation was normal to the interface, in the first and second shear directions in 3D problems, respectively. The Macaulay brackets <-> signify that a pure compressive deformation or stress state did not cause damage.

After fracture initiation occurred, the Kenane–Benzeggagh fracture criterion (Kenane and Benzeggagh, 1997) was utilized to model fracture propagation with continuous rock damage. This criterion assumed that the critical fracture energies along the first and second shear directions were the same, which could be expressed as:

$$G_{n}^{C} + \left(G_{s}^{C} - G_{n}^{C}\right) \left\{ \frac{G_{s} + G_{t}}{G_{n} + G_{s} + G_{t}} \right\}^{\eta} = G^{C}$$
 (2)

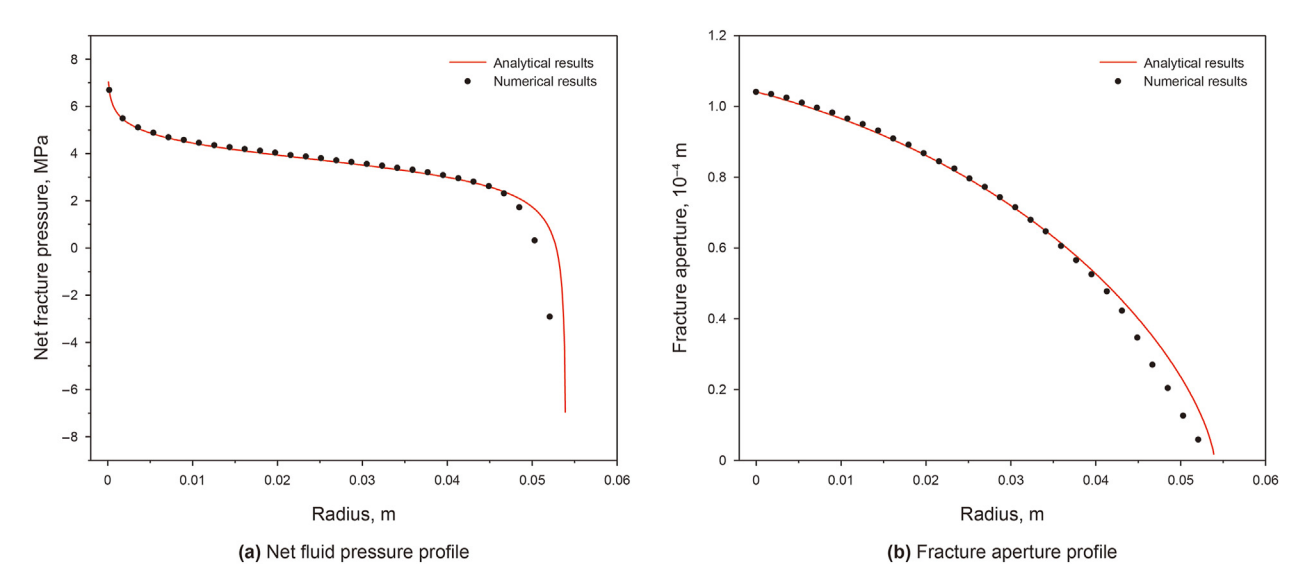


Fig. 5. Comparison for the simulated and analytical solutions.

Table 2 Input parameters for simulation examples.

Category	Parameter	Value
Reservoir layer	Young's modulus E _R , GPa	14.5
	Poisson's ratio $\nu_{\rm R}$	0.15
	Vertical stress $\sigma_{V,R}$, MPa	10-20
	Minimum principle horizontal stress $\sigma_{h,R}$, MPa	10-18
	Maximum principle horizontal stress $\sigma_{H,R}$, MPa	20
Cohesive zone in reservoir layer	Normal nominal stress $t_{n,R}$, MPa	3
	1st shear nominal stress $t_{s,R}$, MPa	30
	2nd shear nominal stress $t_{t,R}$, MPa	30
	Normal fracture energy $G_{n,R}$, Pa·m	100
	1st shear fracture energy $G_{S,R}$, Pa·m	3000
	1st shear fracture energy $G_{t,R}$, $Pa \cdot m$	3000
Barrier layer	Young's modulus $E_{\rm B}$, GPa	34.5
	Poisson's ratio $\nu_{\rm B}$	0.2
	Vertical stress $\sigma_{V,B}$, MPa	10-20
	Minimum principle horizontal stress $\sigma_{h,B}$, MPa	10-18
	Maximum principle horizontal stress $\sigma_{H,B}$, MPa	20
Cohesive zone in barrier layer	Normal nominal stress $t_{n,B}$, MPa	6
	1st shear nominal stress $t_{s,B}$, MPa	60
	Normal nominal stress $t_{t,B}$, MPa	60
	Normal fracture energy $G_{n,B}$, Pa \cdot m	200
	1st shear fracture energy $G_{s,B}$, Pa·m	6000
	1st shear fracture energy $G_{t,B}$, Pa·m	6000

where η is a material parameter; G_n , G_s , and G_t are the fracture energies in the normal, the first and second directions, respectively.

2.2. The fluid flow

The fluid was hypothesized to be incompressible. Newtonian fluid and fluid flow comprise tangential flow within the fracture and normal flow across the fracture. The lubrication equation, which was derived from Poiseuille's law, governed the tangential flow.

$$q = \frac{w^3}{12u} \nabla p \tag{3}$$

where q is the fluid flux of the tangential flow; ∇p is the fluid pressure gradient along the fracture; w is the fracture opening; μ is the fluid viscosity.

The normal flow was defined as (Abaqus, 2014)

$$\begin{cases}
q_t = c_t(p_i - p_t) \\
q_b = c_b(p_i - p_b)
\end{cases}$$
(4)

where $c_{\rm t}$ and $c_{\rm b}$ define the corresponding fluid leak-off coefficients; $p_{\rm i}$ is the fluid pressure within the cohesive element gap; $p_{\rm t}$ and $p_{\rm b}$ are the pore pressures on the top and bottom surfaces, respectively; $q_{\rm t}$ and $q_{\rm b}$ are the normal flow rates into the top and bottom surfaces of the cohesive elements, respectively, which reflect the leak-off through the fracture surfaces into the adjacent porous and permeable rock material. For the impermeable rock in this paper, there was no leak-off and $q_{\rm t}=q_{\rm b}=0$.

2.3. The contact friction

Fictional sliding would occur over the contacting fracture surfaces if the magnitude of the frictional shear stress, $\bar{\tau}_s$, reached the frictional shear strength. The Coulomb friction law with a shear

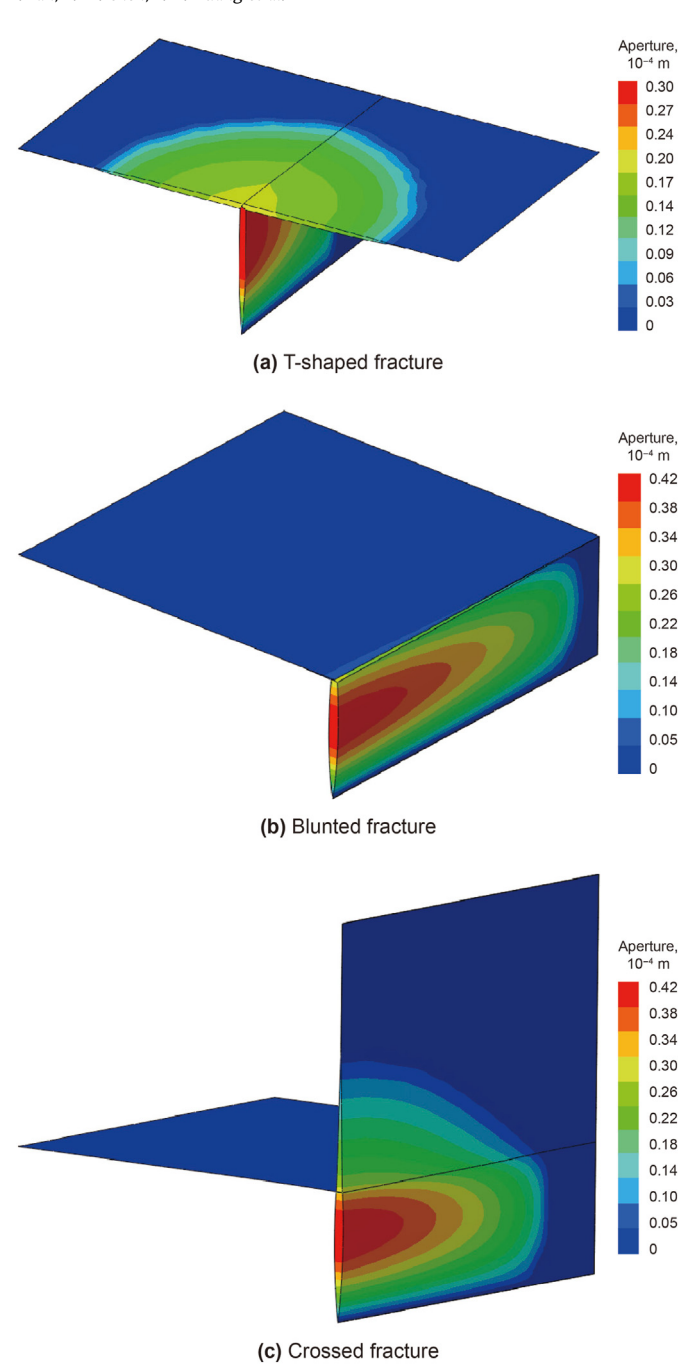


Fig. 6. Typical fracture geometry after simulation.

stress limit, $\overline{\tau}_{max}$, was applied to the failed but contacting surfaces of the fracture in shear or mixed mode, where the shear slippage occurred when the relationship is as follows:

$$|\overline{\tau}_{s}| = \begin{cases} \eta \sigma_{n} & (\eta \sigma_{n} \leq \overline{\tau}_{max}) \\ \overline{\tau}_{max} & (\eta \sigma_{n} \geq \overline{\tau}_{max}) \end{cases}$$
 (5)

where η is the coefficient of friction; and σ_n is the normal contact stress.

3 Model construction and validation

3.1. Model construction

A two-layered model consisting of upper and lower layers with weak interfaces between them is established. A pre-existing HF is defined as oriented orthogonal to the interface. In order to improve the computational efficiency and convergence of the three-dimensional model (Haddad and Kamy, 2016), the model was set to laboratory scale (30 cm \times 30 cm \times 15 cm), as shown in Fig. 3. The model is symmetrical with respect to the x-z plane. In the model, the lower medium is a reservoir rock, and the upper medium is a barrier rock layer. The injection point is positioned in the lower reservoir formation of the HF. An incompressible Newtonian fluid is then injected at a consistent pumping rate. As a result, the HF is initiated and propagates hydraulically due to the pressure exerted by the fluid. The boundary planes are subjected to constant displacement boundary conditions in this model.

Due to the tiny size of the model and its brief period of fracturing, the leakage of fracturing fluid is ignored and the interaction between pore fluid and solid in bedrock is not taken into account. The model is discretized into a rock domain with 46,410 elements (8-node linear brick). The HF and GL are defined by 16,874 elements (12-node displacement and pore pressure, three-dimensional cohesive element). The meshes in the vicinity of the HF and GL are refined to improve the calculation accuracy and the convergent validation. The model utilizes two arrays of cohesive components to simulate the HF and GL. These arrays are blended together to ensure that the injected fluid flows in a transverse and perpendicular manner to the fracture routes (Chen et al., 2017; Haddad and Kamy, 2016).

3.2. Model verification

The reliability and accuracy of the cohesive zone method for modeling multiple fracture propagation have been verified by previous studies (Chen et al., 2017; Haddad and Kamy, 2016; Feng and Gray, 2018). In this part, the model's reliability is benchmarked against a relevant analytical solution before simulating the interaction behavior between HF and GL. The verification problem involves a circular HF propagating of homogeneous rock in a viscosity-dominated regime with no leak-off (Savitski and Detournay, 2002). The domain's dimensions are $30 \text{ cm} \times 30 \text{ cm} \times 15 \text{ cm}$. The specific input parameters are shown in Table 1.

Fig. 4 shows a visualization of the fracture aperture when the radius has attained 0.0524 m. The net fluid pressure profile and fracture aperture profile are depicted in Fig. 5. Fig. 5 also includes an analytical benchmark from Savitski and Detournay (2002). The compared results exhibited high consistency, with a minor variance in the vicinity of the HF tip. The mismatch observed at a short distance near the fracture tip can be attributed to the fact that the numerical source had a limited size, in contrast to the assumption made in the analytical solution that it was a point source. Near the leading edge, the finite initial aperture allows seepage ahead of the fracture tip. By contrast, the theoretical solution proposed by Zhang and Dontsov (2018) had no initial aperture and therefore no seepage.

4. Results and analysis

Based on the simulation model established above, the HF height growth behavior penetrating GL was investigated. The specific simulation parameters are shown in Table 2. This paper focused on the law of height growth under the combined influence of GL

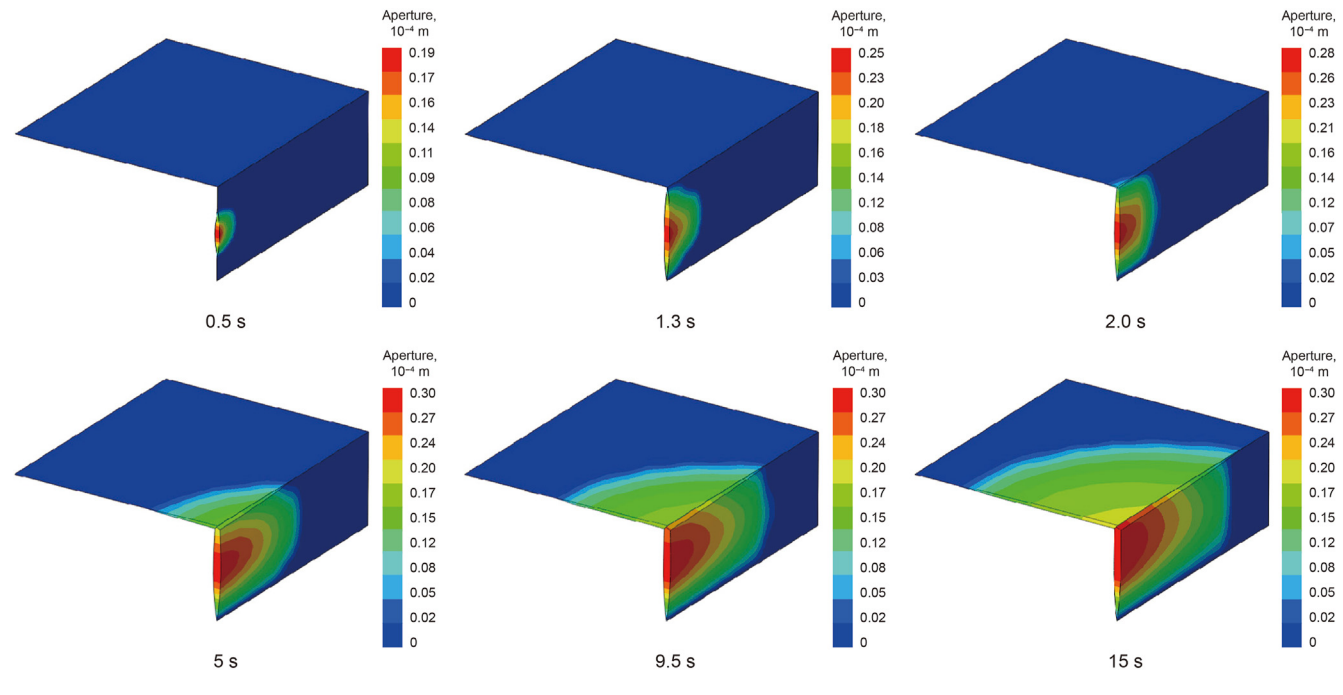


Fig. 7. Evolution of T-shaped fracture.

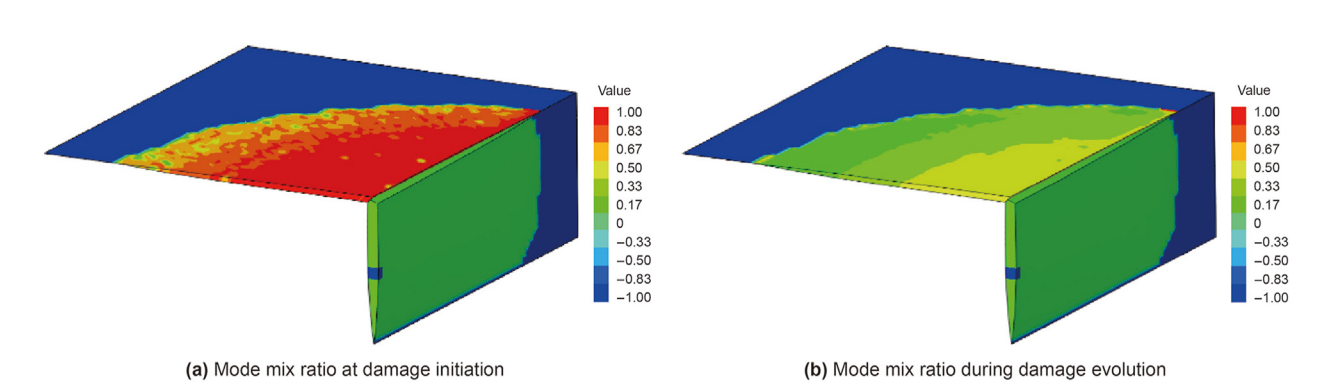


Fig. 8. T-shaped fracture damage mode in initial and evolutionary processes.

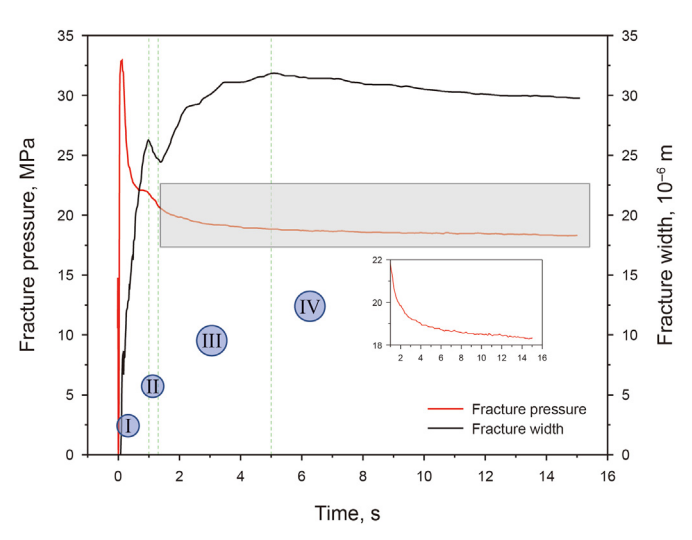


Fig. 9. Evolutions of fluid pressure and fracture width in initiation point for T-shaped fracture.

properties and in-situ stress. In all the examples, the injection rate and the fracturing fluid viscosity are consistent (the injection rate is 6 mL/min, and the viscosity is 200 mPa·s)

For layered strata, the influence of in-situ stress on the fracture propagation behavior and penetration could be classified using two parameters: the interlayer stress difference coefficient and the vertical stress difference coefficient.

$$\zeta_{h} = \left(\sigma_{h,B} - \sigma_{h,R}\right) / \sigma_{h,R} \tag{6}$$

$$\zeta_{V} = \left(\sigma_{V,R} - \sigma_{h,R}\right) / \sigma_{h,R} \tag{7}$$

where ζ_h is the coefficient of interlayer stress difference; ζ_v is the coefficient of vertical stress difference; $\sigma_{h,B}$ is the minimum horizontal stress for the upper barrier layer; $\sigma_{h,R}$ is the minimum horizontal stress for the lower reservoir layer; $\sigma_{v,R}$ is the vertical stress.

The break pattern for the GL included tensile fracture, shear fracture, and tensile-shear complex fracture, which were mainly controlled by tensile and shear strength (Gu et al., 2011; Li S.B. et al., 2017). In this study, in order to comprehensively consider the effects of tensile and shear strength, dimensionless comprehensive

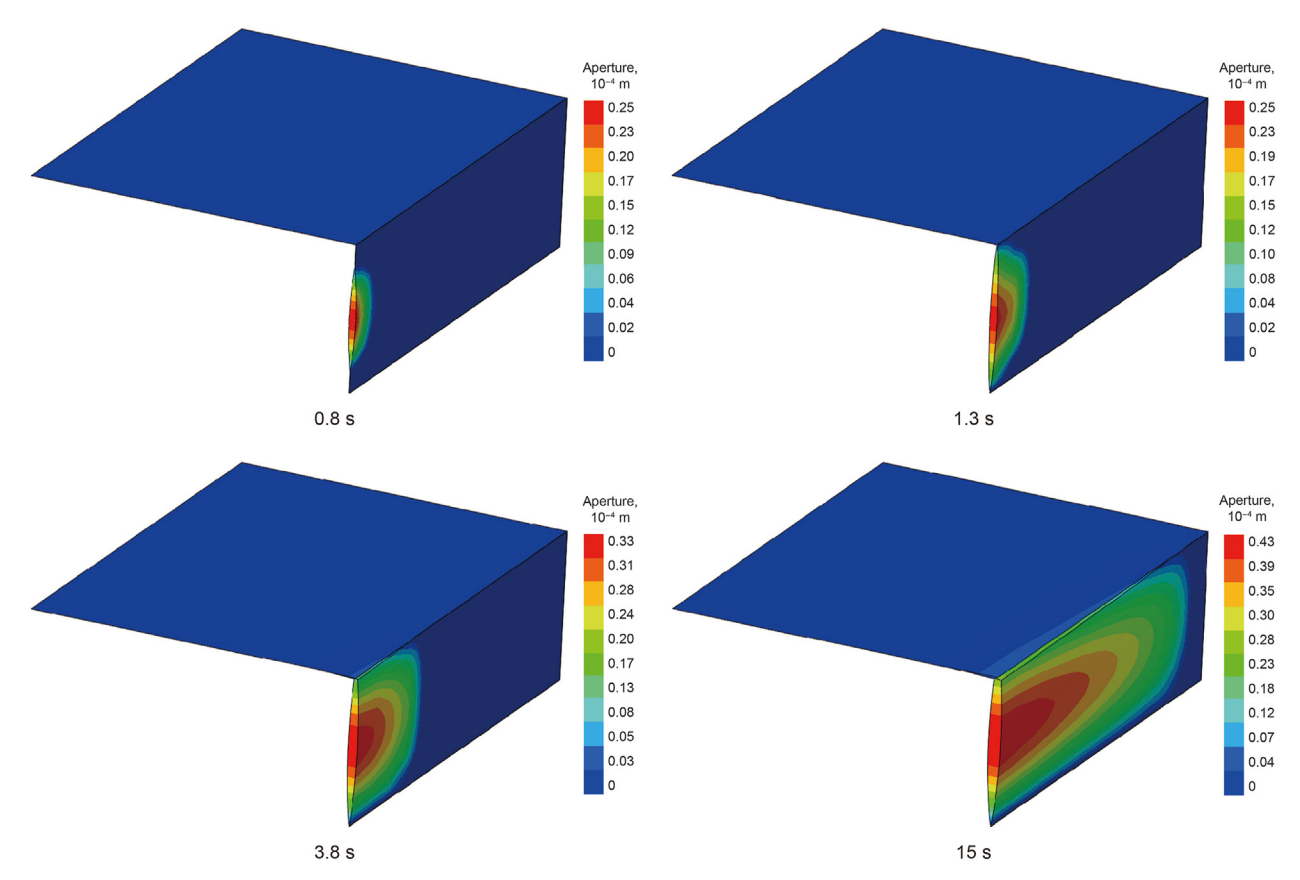


Fig. 10. Evolution of blunted fracture.

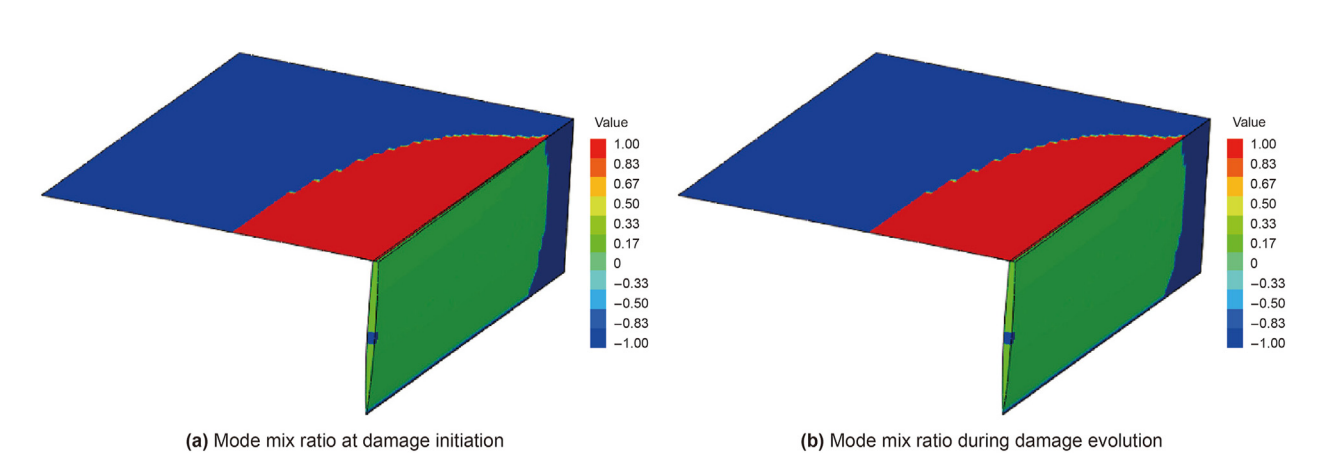


Fig. 11. Blunted fracture damage mode in initial and evolutionary processes.

interface strength was defined, which was

$$\gamma = \left(t_{n,l} / t_{n,R} + \sum_{i} \tau_{l,i} / \tau_{R,i}\right) / 3 \tag{8}$$

where $t_{\rm n,l}$ is the normal nominal stress for GL; $t_{\rm n,R}$ is the normal nominal stress for HF in reservoir layer; i is an index for the first and second shear stress; $t_{\rm l,i}$ is the first and second shear nominal stress for GL; $\tau_{\rm R,i}$ is the first and second shear nominal stress for HF in reservoir layer.

4.1. Results

Under different in-situ stress and interface strength conditions, according to the different interactions between HF and GL, three types of typical fracture patterns were finally presented: T-shaped fracture, blunted fracture, and crossed fracture, as shown in Fig. 6.

4.1.1. T-shaped fracture

Fig. 7 shows the evolution of the T-shaped fracture over time. When HF propagated from the lower reservoir to GL, HF expanded in the shape of a disc. When the fracture contacted with GL, the fracture vertical growth was arrested, the height of the fracture stopped expanding, and the length of the fracture gradually

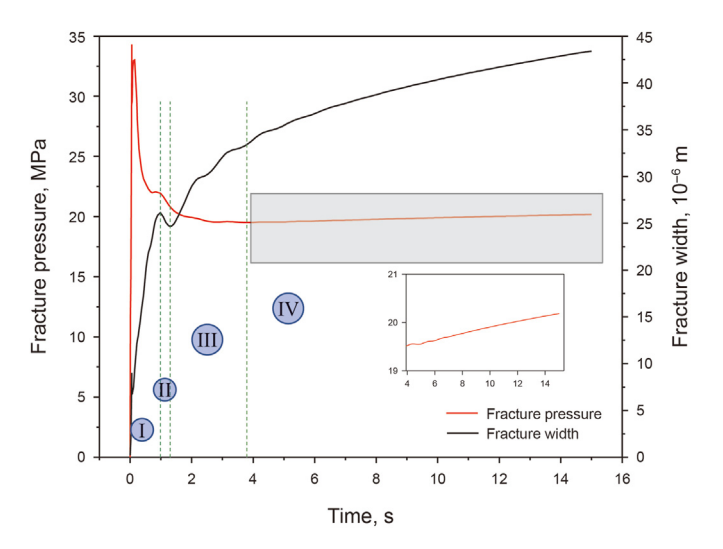


Fig. 12. Evolutions of fluid pressure and fracture width in initiation point for blunted fracture.

expanded forward, which turned into the PKN mode. When the HF contacted the GL, the fracture penetrated into the interface and began to extend further. The fracture shape gradually transferred from circle to ellipse, and HF long axis was along the longitudinal direction of the main HF. The example has an interface strength γ of 0.2, a vertical stress difference coefficient ζ_V of 0.1, and an interlayer stress difference coefficient ζ_h of 0.

The fracture modes in the process of fracture initiation and propagation could be judged by outputting the values of the cohesive units, respectively (Abaqus, 2014). When its value is -1, the unit was not damaged; when the value was 0-0.5, the unit was mainly damaged by tension; when the value was 0.5-1, the unit was mainly damaged by shear (Abaqus, 2014). According to Fig. 8, the initiation and propagation of the main HF were characterized by tensile failure, while shear initiation first occurred for the GL. With the continuous inflow of fracturing fluid, the fluid pressure in the fracture increased, and the cohesive units opened and gradually turned into tensile fractures.

By extracting the pressure and fracture width of the injection point, the variation law of pressure and fracture width during the evolution of T-shaped fractures was studied, as shown in Fig. 9. According to the evolution law of fractures, HF propagation could be divided into four stages (see Fig. 9): HF expanded in reservoirs; HF tip met GL; HF tip blunted; and horizontal fracture propagated. In stage 1, the injection pressure decreased gradually, while the fracture width increased. In stage 2, the injection pressure and fracture width dropped abruptly. In stage 3, the injection pressure decreased and the fracture width increased. In stage 4, the injection pressure and fracture width decreased.

4.1.2. Blunted fracture

Fig. 10 depicts the progression of the blunted fracture. When the HF propagated from the lower reservoir to the GL, it grew in the shape of a disk; when the HF came into contact with the interface, the fracture tip gradually blunted, the fracture height stopped rising, and the fracture length continued to extend, resulting in a PKN-type growth mode.

When the HF contacted the GL, the GL began to extend. The fracture shape was always elliptical, whose long axis was along the longitudinal direction of the main HF. The example has an interface strength γ of 0.1, a vertical stress difference coefficient ζ_V of 0.5, and an interlayer stress difference coefficient ζ_h of 0.

Fig. 11 shows the fracture mode of the blunted fracture. The results showed that the HF fracture type in the process of initiation and propagation was tensile, while the GL fracture type in the process was shear.

Fig. 12 shows the evolution rule of blunted fracture, and the propagation of HFs could be divided into four stages: HF expanded in reservoirs; HF tip met GL; HF tip got blunted; and vertical fracture propagated. In stage 1, the injection pressure decreased gradually and the fracture width increased. In stage 2, the injection pressure and the fracture width dropped abruptly. In stage 3, the injection pressure decreased and the fracture width increased. In stage 4, the injection pressure increased as predicted by the PKN growth model, and the fracture width increased.

4.1.3. Crossed fracture

Fig. 13 shows the evolution process of the crossed fracture.

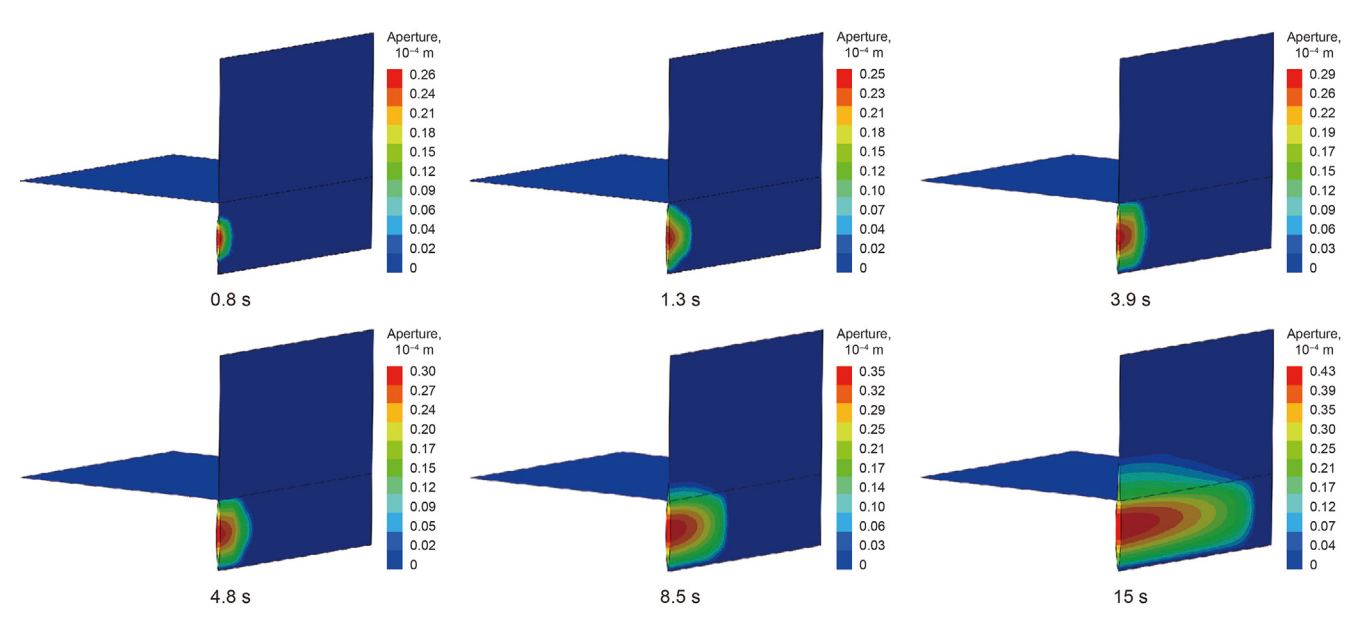


Fig. 13. Evolution of crossed fracture.

-0.33

-0.50

-0.83 -1.00

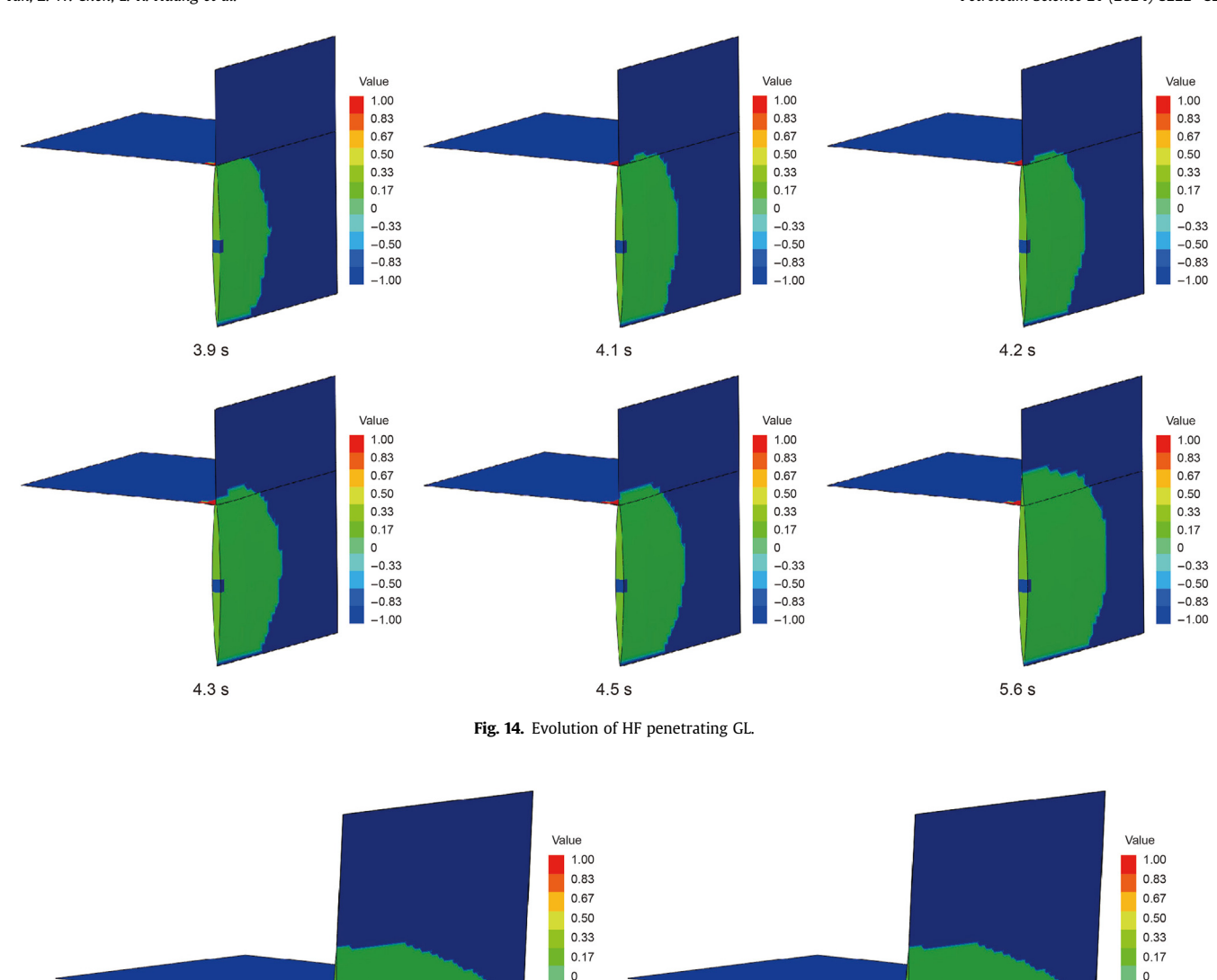


Fig. 15. Crossed fracture damage mode in initial and evolutionary processes.

-0.33

-0.50

-0.83

When the HF started from the lower reservoir and expanded to the GL, it expanded as a disc fracture; when the fracture contacted the GL, the fracture tip first got blunted, the fracture height temporarily stopped expanding, and then continued to expand. The simulation results showed that when the three-dimensional HF extended to the GL, the fracture tip would preferentially be blunted and then preferentially enter the GL from one point on the front edge of the blunted fracture rather than directly penetrated from the original fracture tip. As shown in Fig. 14, this phenomenon was similar to the physical simulation test results observed by Xing et al. (2018a). The example has an interface strength γ of 0.3, the vertical stress difference coefficient $\zeta_{\rm V}$ of 0.5, and the interlayer stress difference coefficient $\zeta_{\rm h}$ of 0.

(a) Mode mix ratio at damage initiation

Fig. 15 shows the fracture mode of the crossed fracture. The results showed that the HF fracture type in the processes of initiation and propagation was tensile, while the GL was hardly damaged. Only a few cohesive elements near the HF were damaged,

and their initiation and propagation were shear.

(b) Mode mix ratio during damage evolution

Fig. 16 shows the evolution rule of blunted fracture, and the expansion of HF could be divided into four stages: HF expanded in reservoirs; HF tip met GL; HF tip got blunted; and HF expanded vertically. In stage 1, the injection pressure decreased gradually, while the fracture width increased. In stage 2, the injection pressure and the fracture width dropped abruptly. In stage 3, the injection pressure decreased and the fracture width increased. In stage 4, the injection pressure and fracture width increased.

Based on the above analysis results, the comparative results of the pore pressure at the injection point, fracture width, intersection characteristics, and failure form for the above three fracture types were carried out, as shown in Table 3. The results indicated that the HF failure type for all three fracture types was tensile, while the initial GL failure type was sheared for all three fracture types. When the HF met GL, the HF for the three types was blunted. Additionally, in the case of the T-shaped fracture, the fracture width of the HF

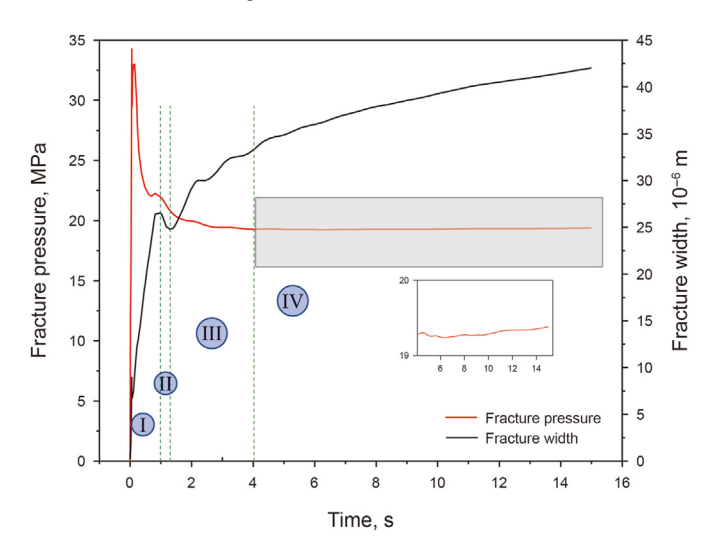


Fig. 16. Evolutions of fluid pressure and fracture width in initiation point for crossed fracture.

decreased during the propagation process of the GL. Considering the construction and fracturing effects, T-shaped fracture reduced the effective transformation volume and hindered the migration of propping agents, which would lead to sand plugging.

4.2. Analysis

According to the condition of the in-situ stress difference between layers, the layered formation could be divided into two types: no interlayer stress difference ($\zeta_h=0$) and with interlayer stress difference ($\zeta_h\neq 0$). In the following two stress conditions, the fracture height growth behavior was analyzed.

4.2.1. No interlayer stress difference $(\zeta_h = 0)$

When there was no interlayer stress difference, the influence of vertical stress difference coefficient and interface strength on fracture height growth was studied by changing the vertical stress and interface parameters. The simulation results are shown in Fig. 17. According to the above three types of fractures, the controlling chart could be divided into three areas: the lower left area was the T-shaped fracture controlling area; the upper left area was blunted fracture controlling area; the upper right area was the crossed fracture controlling area. The simulation results showed that the lower the interface strength was, and the smaller the vertical stress difference coefficient was, the easier it was to form Tshaped fracture. The lower the interface strength was, and the greater the vertical stress difference coefficient was, the easier it was to form blunted fracture. The higher the interface strength was, and the greater the vertical stress difference coefficient was, the easier it was to form crossed fracture.

4.2.2. With interlayer stress difference $(\zeta_h \neq 0)$

When there was an interlayer stress difference, by changing the vertical stress, the minimum horizontal in-situ stress, and the

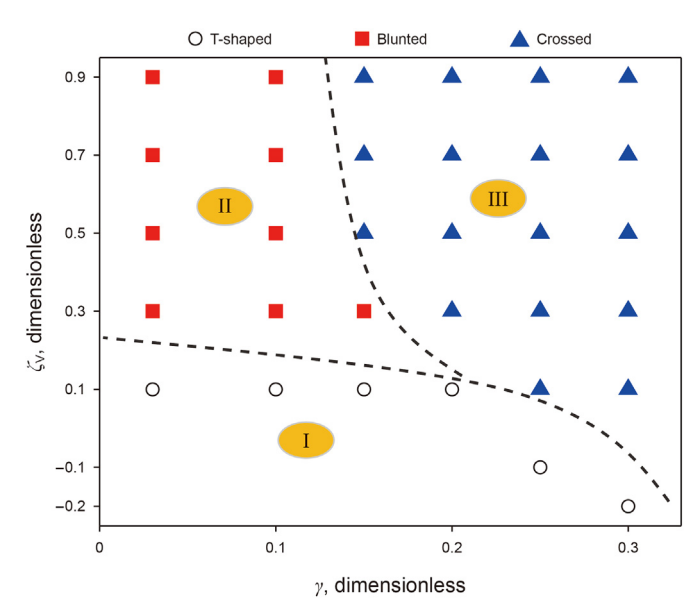


Fig. 17. Simulation results affected by the vertical stress coefficient and interface strength (I: Region of T-shaped fracture; II: Region of blunted fracture; III: Region of crossed fracture).

interface parameters, the influence of three factors, including the interface strength, the vertical stress difference coefficient, and the interlayer stress difference coefficient, on the fracture height growth was studied. As shown in Fig. 18, the shapes of fracture height under the influence of the vertical stress difference coefficient and interlayer stress difference coefficient in different interface strength conditions were given.

According to the three types of fractures, the chart could also be divided into three areas (see Fig. 18(a)): The lower right area was the T-shaped fracture controlling area; the upper right area was the blunted fracture controlling area; and the upper left area was the crossed fracture controlling area. The findings indicated that the lower the interface strength and the smaller the vertical stress difference coefficient, the easier it was to generate a T-shaped fracture. A blunted fracture was more likely to form when the contact strength was low and the vertical stress difference coefficient was high. An increased interface strength and a higher vertical stress difference coefficient resulted in an easier formation of a crossed fracture.

With the decrease in the interface strength (see Fig. 18(a)—(d)), the boundary between the blunted fracture and the crossed fracture (line A in Fig. 18(a)) moved to the left continuously, and the boundary between the T-shaped fracture and the crossed fracture (line B in Fig. 18(a)) moved up gradually, indicating that the probability of the crossed fracture under the low interface strength decreased gradually. The results showed that when the interface strength was less than 0.1 (see Fig. 18(e)—(f)), only T-shaped fractures and blunted fractures could be formed, and no crossed fractures could be found. When the interface strength was 0.2—0.25, the formation of a T-shaped fracture was only determined by the vertical stress difference coefficient, which was independent of the

Table 3Comparison of propagation characteristic for three fracture patterns.

Fracture pattern	Extension pressure	Fracture aperture	Intersection characteristic	Failure mode of HF	Failure mode of GL
T-shaped fracture Blunted fracture Crossed fracture	Decrease Increase	Decrease Increase	Passivation for fracture tip	Tensile	Shear first and then tensile Shear

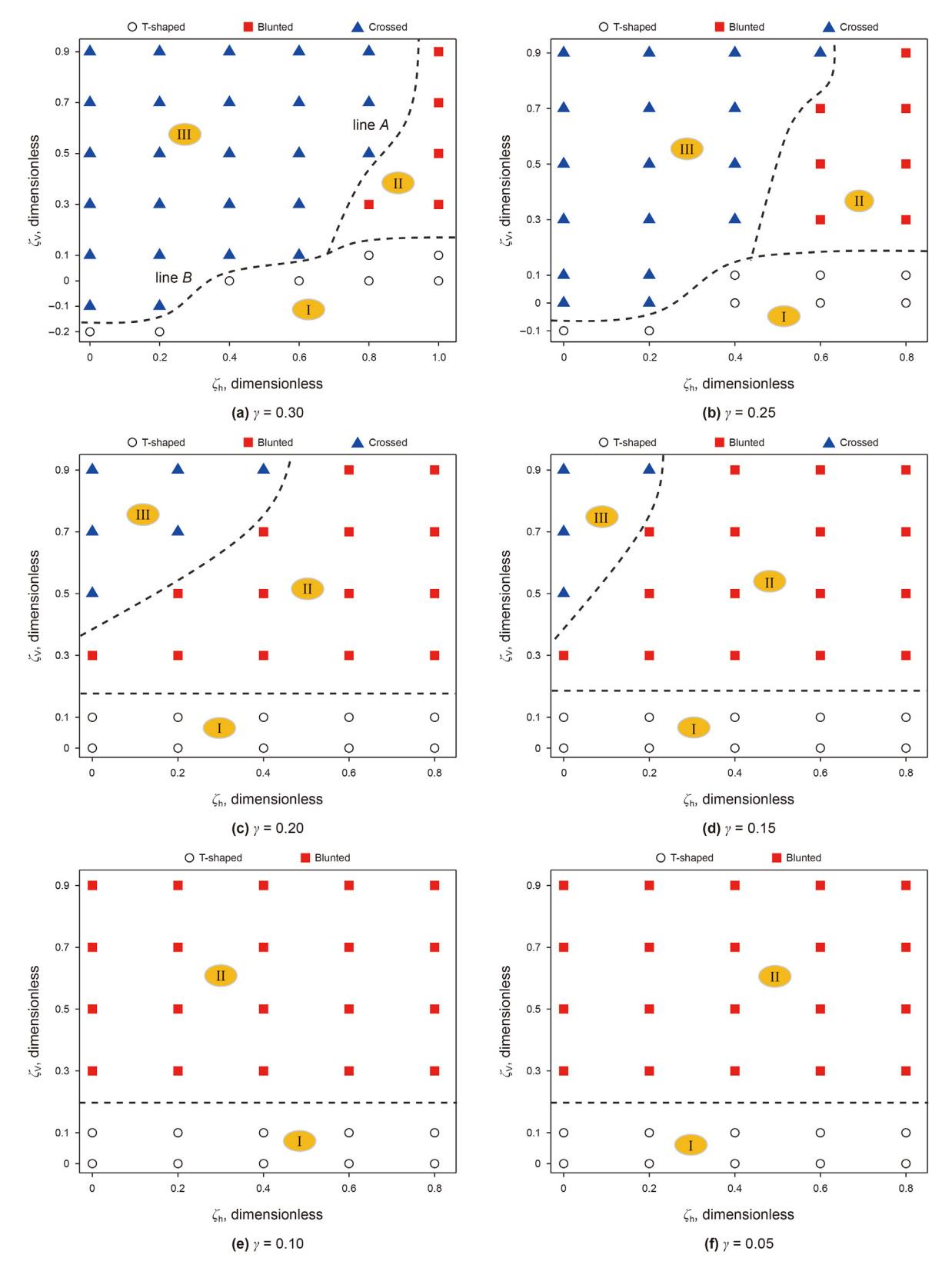


Fig. 18. Simulation results affected by vertical stress coefficient and horizontal stress coefficient under different interface strength.

interlayer stress difference coefficient. In addition, T-shaped fractures could only be formed when the vertical stress coefficient was less than 0.1-0.3, and only blunted fractures or crossed fractures

could be formed when the vertical stress coefficient was greater than this value.

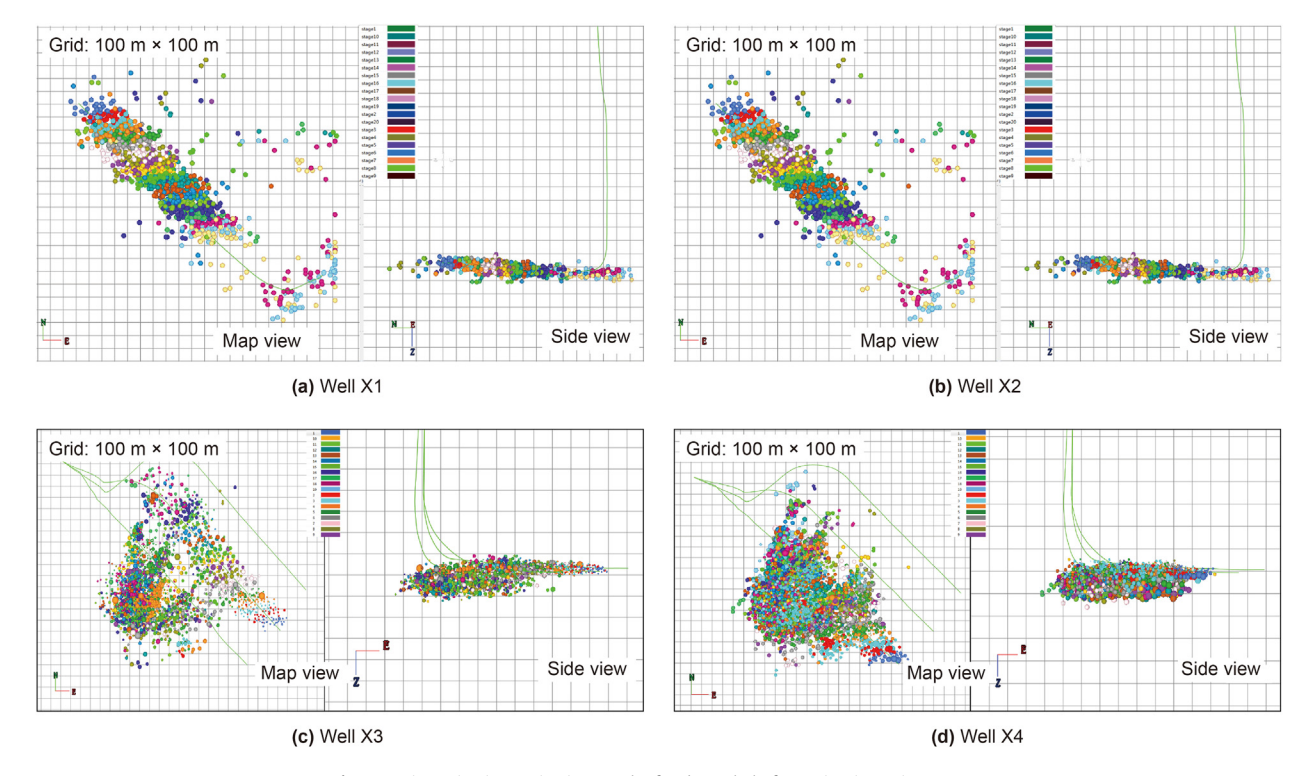


Fig. 19. Microseismic monitoring results for deep shale formation in Weiyuan area.



Fig. 20. Shale cores from different depths.

5. Significance and applicability of results

Shale fracturing in the Sichuan Basin in China showed that as the depth of the reservoir increased, it became increasingly challenging to expand and create a network of fractures (Jiang et al., 2017a, 2017b). Fig. 19 showed the real-time micro-seismic monitoring results of various typical deep shale fracturing wells in Sichuan, China. The fracture height monitoring data of well X using non-radioactive tracer haydite revealed that the real fracture height was extremely difficult to propagate, and the effective fracture height was only 11 m, which was significantly less than the expected fracture height (Tan et al., 2021).

In addition, our prior research (Tan et al., 2020) yielded a great number of laboratory data for deep and mid-depth shale. The findings indicated that the primary fracture observed in mid-depth shale was a vertical fracture, resulting in a final fracture pattern characterized by a fishbone fracture network with transverse fractures as the primary fractures (Tan et al., 2017). On the other hand, the main fracture observed in deep shale was a horizontal fracture, leading to a final fracture pattern characterized by a step fracture network with horizontal fractures as the primary fractures (Tan et al., 2020). Three patterns of HF network in vertical plane were summed up based on the lateral distribution range of HF in longitudinal sections. As the depth of the shale reservoir increases,

the type of HF network in the vertical direction progressively transforms from a small horizontal sweep to a large horizontal sweep.

The variation in vertical fracture geometry between deep and mid-depth shale reservoirs was clarified using the aforementioned on-site fracturing data and laboratory experimental results, but the reason for this has yet to be discovered. Based on the numerical simulation presented in this research and considering the specific features of deep and mid-depth shale reservoirs in Sichuan, a novel theoretical explanation can be proposed.

Prior research (Zeng et al., 2016; Jiang et al., 2017a, 2017b) has demonstrated that the properties of deep and mid-depth shale reservoirs in the Sichuan Basin are distinct. Small vertical stress difference coefficients characterized the mid-depth buried shale in the Sichuan Basin. Because of the low tectonic compression during sedimentation, reservoir bedding planes and NFs were highly cemented (Jiang et al., 2017a). Deep shale reserves were deeply buried, and the vertical stress differential coefficient was high. The formation was highly compressed in the post-deposition period, resulting in a large number of bedding planes and NFs with extremely low cementation strength compared with mid-depth shale (Jiang et al., 2017a). The clear distinctions between deep and mid-depth shales can also be detected from the cores extracted from two wells in the Sichuan Basin, as shown in Fig. 20.

Without accounting for the difference in stress between layers (as in the case of a shale reservoir), the ability of HF to penetrate the bedding plane vertically depends on both the strength of the interface and the coefficient of vertical stress difference coefficient (see Fig. 17). For mid-depth shale, the bedding plane has strong cementation strength. So, even with a relatively modest vertical stress difference coefficient, it was able to penetrate the interface and generate a primary transverse fracture, with a considerable final fracture height. The cementation strength of the bedding layer in deep shale was exceptionally weak. Despite the presence of a significant vertical stress difference coefficient, HF was unable to penetrate the interface, resulting in a limited fracture height.

This study revealed the factors contributing to the difference in fracture types between deep and mid-depth shale reservoirs in Sichuan, as well as the formation mechanism of horizontal fractures in deep shale reservoirs.

6. Conclusions

A three-dimensional finite element model with HF and GL was developed using the cohesive zone approach, taking into account the influence of interface cementation strength and friction characteristics. A quantitative analysis was conducted to study the propagation characteristics of HF in three-dimensional space. The controlling charts for fracture height growth were developed after conducting a thorough analysis of critical parameters such as interface strength, interlayer stress difference coefficient, and vertical stress difference coefficient. The findings can be summarized as follows.

(1) Three distinct types of vertical propagation for HF were identified based on the various modes of interaction between HF and GL: T-shaped fracture, blunted fracture, and crossed fracture. The characteristics of injection pressure, fracture width, and fractured mode were compared for the three fracture kinds, and it was discovered that the curve of fluid pressure at injection point and HF width could be split into four characteristic stages. HF passivation could occur at the fracture tip when the HF reached the GL in these three types of fractures.

- (2) The fracture height geometry was determined by the interface strength, the vertical stress difference coefficient, and the interlayer stress difference coefficient. A T-shaped fracture was more likely to form when the interface strength was lower and the vertical stress difference coefficient was smaller. A blunted fracture formed more easily when the vertical stress difference coefficient was greater and the interface strength was lower. Greater interface strength and a higher vertical stress difference coefficient facilitated the formation of a crossing fracture. A T-shaped fracture could only occur if the vertical stress difference coefficient was less than a crucial value of 0.1–0.3.
- (3) The likelihood of HF traversing the interface decreased as the interface strength diminished. When the interface strength was below 0.1, only two forms of fractures, specifically T-shaped and blunted, were observed, and HF was unable to pass through the interface.
- (4) The simulation results elucidated that as the depth of shale reservoirs increased in the Sichuan Basin, the fracture height patterns underwent a progressive transition from a tallshaped fracture with a small horizontal extent to a short fracture with a big horizontal extent.

CRediT authorship contribution statement

Peng Tan: Writing — original draft, Investigation, Conceptualization. **Zhao-Wei Chen:** Writing — review & editing, Investigation. **Liu-Ke Huang:** Writing — original draft, Supervision. **Qing Zhao:** Writing — review & editing, Visualization. **Sha-Rui Shao:** Writing — review & editing, Investigation.

Declaration of competing interest

The authors declare that they have no conflicts of interest.

Acknowledgements

The authors sincerely appreciate the funding provided by the National Natural Science Foundation of China (No. 52334001, No. 42372337), National Key Research and Development Program of China (No. SQ2023YFE0100562), CPET Industrialization Fund Project (No. CPETCY202417), and Natural Science Starting Project of SWPU (No. 2022QHZ009).

References

Abaqus, 2014. User's manual. Dassault Systems, Version 6.14.

Ahmed, U., 1984. A practical hydraulic fracturing model simulating necessary fracture geometry, fluid flow and leakoff and proppant transport. In: SPE/DOE/GRI Unconventional Gas Recevory Symposium. https://doi.org/10.2118/12880-MS

Altammar, M.J., Agrawal, S., Sharma, M.M., 2019. Effect of geological layer properties on hydraulic fracture initiation and propagation: an experimental study. SPE J. 24 (2), 757–794. https://doi.org/10.2118/184871-PA.

Chen, Z.X., Jeffrey, R.G., Zhang, X., et al., 2017. Finite-element simulation of a hydraulic fracture interacting with a natural fracture. SPE J. 22 (1), 219–234. https://doi.org/10.2118/176970-PA.

Chuprakov, D.A., Prioul, R., 2015. Hydraulic fracture height containment by weak horizontal interface. In: SPE Hydraulic Fracturing Technology Conference. https://doi.org/10.2118/SPE-173337-MS.

Feng, Y.C., Gray, K.E., 2018. Modeling lost circulation through drilling-induced fractures. SPE J. 23, 205—223. https://doi.org/10.2118/187945-PA.

Fu, W., Ames, B.C., Bunger, A.P., et al., 2016. Impact of partially cemented and non-persistent natural fractures on hydraulic fracture propagation. Rock Mech. Rock Eng. 49, 4519–4526. https://doi.org/10.1007/s00603-016-1103-0.

Fu, W., Savitski, A.A., Andrew, P.B., 2018. Analytical criterion predicting the impact of natural fracture strength, height and cemented portion on hydraulic fracture growth. Eng. Fract. Mech. 204, 497–516. https://doi.org/10.1016/ j.engfracmech.2018.10.002.

Fung, R.L., Vijayakumar, S., Cormack, D.E., 1987. Calculation of vertical fracture containment in layered formations. SPE Form. Eval. 2 (4), 518–522. https:// doi.org/10.2118/14707-PA.

- Geertsma, J., De, Klerk F., 1969. A rapid method of predicting width and extent of hydraulically induced fractures. J. Petrol. Technol. 21 (12), 1–571. https:// doi.org/10.2118/2458-PA.
- Goldstein, Osipenko, N.M., 2015. Initiation of a secondary fracture across a frictional interface. Eng. Fract. Mech. 140, 92–105. https://doi.org/10.1016/j.engfracmech.2015.03.036.
- Gu, H., Weng, X., Lund, J., et al., 2011. Hydraulic fracture crossing natural fracture at non-orthogonal angles, a criterion, its validation and applications. In: SPE Hydraulic Fracturing Technology Conference and Exhibition. https://doi.org/ 10.2118/139984-MS.
- Gu, H., Weng, X., Land, J., et al., 2012. Hydraulic fracture crossing natural fracture at nonorthogonal angles: a criterion and its validation. SPE Prod. Oper. 27 (1), 20–26. https://doi.org/10.2118/139984-PA, 2012.
- Guo, D., Zhang, S., Li, T., et al., 2018. Mechanical mechanisms of T-shaped fractures, including pressure decline and simulated 3D models of fracture propagation. J. Nat. Gas Sci. Eng. 50, 1–10. https://doi.org/10.1016/j.jngse.2017.11.018.
- Guo, J.C., Luo, B., Lu, C., et al., 2017. Numerical investigation of hydraulic fracture propagation in a layered reservoir using the cohesive zone method. Eng. Fract. Mech. 186, 195–207. https://doi.org/10.1016/j.engfracmech.2017.10.013.
- Haddad, M., Kamy, S., 2016. XFEM-based CZM for the simulation of 3D multiplecluster hydraulic fracturing in quasi-brittle shale formations. Rock Mech. Rock Fng. 49 (12) 4731–4748. https://doi.org/10.1007/s00603-016-1057-2
- Eng. 49 (12), 4731–4748. https://doi.org/10.1007/s00603-016-1057-2. Haddad, M., Du, J., Vidal, Gilbert S., 2017. Integration of dynamic microseismic data with a true 3D modeling of hydraulic-fracture propagation in the Vaca Muerta Shale. SPE J. 22 (6), 1714–1738. https://doi.org/10.2118/179164-PA.
- Han, S.C., Gao, Q., Yan, X.C., et al., 2024. Thermally-induced cracking behaviors of coal reservoirs subjected to cryogenic liquid nitrogen shock. J. Rock Mech. Geotech. Eng. https://doi.org/10.1016/j.jrmge.2023.12.018 (in press).
- He, R., Yang, J., Li, L., et al., 2023. Investigating the simultaneous fracture propagation from multiple perforation clusters in horizontal wells using 3D block discrete element method. Front. Earth Sci. 11, 1115054. https://doi.org/10.3389/feart.2023.1115054.
- Hou, B., Chang, Z., Fu, W.N., et al., 2019. Fracture initiation and propagation in a deep shale gas reservoir subject to an alternating-fluid-injection hydraulic fracturing treatment. SPE J. 24 (4), 1839—1855. https://doi.org/10.2118/195571-PA.
- Huang, B.X., Liu, J.W., 2018. Fully three-dimensional propagation model of horizontal borehole hydraulic fractures in strata under the effect of bedding planes. Energy Explor. Exploit. 36 (5), 1189–1209. https://doi.org/10.1177/0144598717754101.
- Huang, L.K., Liu, J.J., Zhang, F.S., et al., 2019. Exploring the influence of rock inherent heterogeneity and grain size on hydraulic fracturing using discrete element modeling. Int. J. Solid Struct. 176, 207–220. https://doi.org/10.1016/ j.ijsolstr.2019.06.018.
- Huang, L.K., Liu, J.J., Zhang, F.S., et al., 2020. 3D lattice modeling of hydraulic fracture initiation and near-wellbore propagation for different perforation models. J. Petrol. Sci. Eng. 191, 107169. https://doi.org/10.1016/j.petrol.2020.107169.
- Huang, L.K., Dontsov, E., Fu, H.F., et al., 2022. Hydraulic fracture height growth in layered rocks: perspective from DEM simulation of different propagation regimes. Int. J. Solid Struct. 238, 111395. https://doi.org/10.1016/ j.ijsolstr.2021.111395.
- Huang, L.K., He, R., Yang, Z.Z., et al., 2023a. The non-plane initiation and propagation mechanism of multiple hydraulic fractures in tight reservoirs considering stress shadow effects. Eng. Fract. Mech. 292, 109570. https://doi.org/10.1016/ j.engfracmech.2023.109570.
- Huang, L.K., He, R., Yang, Z.Z., et al., 2023b. Exploring hydraulic fracture behavior in glutenite formation with strong heterogeneity and variable lithology based on DEM simulation. Eng. Fract. Mech. 278, 109020. https://doi.org/10.1016/ j.engfracmech.2022.109020.
- Huang, L.K., Liao, X.C., Fan, M., et al., 2024. Experimental and numerical simulation technique for hydraulic fracturing of shale formations. Advances in Geo-Energy Research 13 (2), 83–88. https://doi.org/10.46690/ager.2024.08.02.
- Jeffrey, R.G., Bunger, A.P., 2007. A detailed comparison of experimental and numerical data on hydraulic fracture height growth through stress contrasts. In: SPE Hydraulic Fracturing Technology Conference. https://doi.org/10.2118/106030_PA
- Jiang, T.X., Zhou, J., Zhang, X., et al., 2017a. Overview and prospect of fracture propagation and conductivity characteristics in deep shale gas wells. Scientia Sinica Physica, Mechanica & Astronomica 47 (11), 114603. https://doi.org/ 10.1360/SSPMA2016-00535.
- Jiang, T.X., Bian, X.B., Wang, H.T., et al., 2017b. Volume fracturing of deep shale gas horizontal wells. Nat. Gas. Ind. 37 (1), 90–96. https://doi.org/10.1016/ j.ngib.2017.07.018.
- Kenane, M., Benzeggagh, M.L., 1997. Mixed-mode delamination fracture toughness of unidirectional glass/epoxy composites under fatigue loading. Compos. Sci. Technol. 57 (5), 597–605. https://doi.org/10.1016/S0266-3538(97)00021-3.
- Li, N., Zhang, S.C., Zou, Y.S., 2018. Experimental analysis of hydraulic fracture growth and acoustic emission response in a layered formation. Rock Mech. Rock Eng. 51 (4), 1047–1062. https://doi.org/10.1007/s00603-017-1383-z.
- Li, S.B., Zhang, D.X., Li, X., 2017. A new approach to the modeling of hydraulic-fracturing treatments in naturally fractured reservoirs. SPE J. 22 (4), 1064–1081. https://doi.org/10.2118/181828-PA.
- Li, Y.W., Long, M., Tang, J.Z., et al., 2020. A hydraulic fracture height mathematical

- model considering the influence of plastic region at fracture tip. Petrol. Explor. Dev. 47, 184–195. https://doi.org/10.1016/S1876-3804(20)60017-9.
- Li, Y., Deng, J.G., Liu, W., et al., 2017. Numerical simulation of limited-entry multicluster fracturing in horizontal well. J. Petrol. Sci. Eng. 152, 443–455. https:// doi.org/10.1016/j.petrol.2017.03.023.
- Liu, S.X., Valko, P.P., 2015. An Improved equilibrium-height model for predicting hydraulic fracture height migration in multi-layer formations. In: SPE Hydraulic Fracturing Technology Conference. https://doi.org/10.2118/SPE-173335-MS.
- Luo, H.R., Xie, J., Huang, L.K., et al., 2022. Multiscale sensitivity analysis of hydraulic fracturing parameters based on dimensionless analysis method. Lithosphere 2022. 9708300. https://doi.org/10.2113/2022/9708300.
- Nordgren, R.P., 1972. Propagation of a vertical hydraulic fracture. Soc. Petrol. Eng. J. 12 (4), 306–314. https://doi.org/10.2118/3009-PA.
- Ouchi, H., Foster, J.T., Sharma, M.M., 2017. Effect of reservoir heterogeneity on the vertical migration of hydraulic fractures. J. Petrol. Sci. Eng. 151, 384–408. https://doi.org/10.1016/j.petrol.2016.12.034.
- Oyedokun, O., Schubert, J., 2017. A quick and energy consistent analytical method for predicting hydraulic fracture propagation through heterogeneous layered media and formations with natural fractures: the use of an effective fracture toughness. J. Nat. Gas Sci. Eng. 44, 351–364. https://doi.org/10.1016/ i.ingse.2017.05.001.
- Perkins, T.K., Kern, L.R., 1961. Widths of hydraulic fractures. J. Petrol. Technol. 13 (9), 937–949. https://doi.org/10.2118/89-PA.
- Savitski, A., Detournay, E., 2002. Propagation of a penny-shaped fluid-driven fracture in an impermeable rock: asymptotic solutions. Int. J. Solid Struct. 39, 6311–6337. https://doi.org/10.1016/S0020-7683(02)00492-4.
- Simonson, E.R., About Sayed, A.S., Clifton, R.R.J., 1979. Containment of massive hydraulic fractures. SPE J. 18 (1), 27–32. https://doi.org/10.2118/6089-PA.
- Smith, M.B., Bale, A.B., Britt, L.K., et al., 2001. Layered modulus effects on fracture propagation, proppant placement, and fracture modeling. In: SPE Annual Technical Conference and Exhibition. https://doi.org/10.2118/71654-MS.
- Tan, P., Jin, Y., Han, K., et al., 2017. Analysis of hydraulic fracture initiation and vertical propagation behavior in laminated shale formation. Fuel 206, 482–493. https://doi.org/10.1016/j.fuel.2017.05.033.
- Tan, P., Pang, H.W., Zhang, R.X., et al., 2020. Experimental investigation into hydraulic fracture geometry and proppant migration characteristics for southeastern Sichuan deep shale reservoirs. J. Petrol. Sci. Eng. 184, 106517. https://doi.org/10.1016/j.petrol.2019.106517.
- Tan, P., Jin, Y., Pang, H.W., 2021. Hydraulic fracture vertical propagation behavior in transversely isotropic layered shale formation with transition zone using XFEM-based CZM method. Eng. Fract. Mech. 248, 107707. https://doi.org/ 10.1016/j.engfracmech.2021.107707.
- Tan, P., Fu, S.H., Chen, Z.W., et al., 2023. Experimental investigation on fracture growth for integrated hydraulic fracturing in multiple gas bearing formations. Geoenergy Science and Engineering 231, 212316. https://doi.org/10.1016/j.geoen.2023.212316.
- Tang, J.Z., Wu, K., 2018. A 3-D model for simulation of weak interface slippage for fracture height containment in shale reservoirs. Int. J. Solid Struct. 144–145, 248–264. https://doi.org/10.1016/j.ijsolstr.2018.05.007.
- Teufel, L.W., Clark, J.A., 1984. Hydraulic fracture propagation in layered rock: experimental studies of fracture containment. SPE J. 24 (1), 19–32. https://doi.org/10.2118/9878-PA.
- van Eekelen, H.A.M., 1982. Hydraulic fracture geometry: fracture containment in layered formations. SPE J. 22 (3), 341–349. https://doi.org/10.2118/9261-PA.
- Wang, T., Hu, W., Elsworth, D., et al., 2017. The effect of natural fractures on hydraulic fracturing propagation in coal seams. J. Petrol. Sci. Eng. 150, 180–190. https://doi.org/10.1016/j.petrol.2016.12.009.
- Warpinski, N.R., Clark, J.A., Schmidt, R.A., et al., 1982. Laboratory investigation on the effect of in-situ stresses on hydraulic fracture containment. SPE J. 22 (3), 333–340. https://doi.org/10.2118/9834-PA.
- Xing, P.J., Yoshiokab, K., Adachib, J., et al., 2017. Laboratory measurement of tip and global behavior for zero-toughness hydraulic fractures with circular and bladeshaped (PKN) geometry. J. Mech. Phys. Solid. 104, 172–186. https://doi.org/ 10.1016/j.imps.2017.04.013.
- Xing, P.J., Yoshiokab, K., Adachib, J., et al., 2018a. Laboratory demonstration of hydraulic fracture height growth across weak discontinuities. Geophysics 83 (2), 93–105. https://doi.org/10.1190/geo2016-0713.1.
- Xing, P.J., Yoshiokab, K., Adachib, J., et al., 2018b. Lattice simulation of laboratory hydraulic fracture containment in layered reservoirs. Computer and Geotechnics 100, 62–75. https://doi.org/10.1016/j.compgeo.2018.03.010.
- Yan, X., Yu, H.T., 2022. Numerical simulation of hydraulic fracturing with consideration of the pore pressure distribution based on the unified pipe-interface element model. Eng. Fract. Mech. 275, 108836. https://doi.org/10.1016/i.engfracmech.2022.108836.
- Yan, X., Sun, Z.Z., Li, S.C., et al., 2019. Quantitatively assessing the pre-grouting effect on the stability of tunnels excavated in fault zones with discontinuity layout optimization: a case study. Front. Struct. Civ. Eng. 13 (6), 1393–1404. https:// doi.org/10.1007/s11709-019-0563-1.
- Yan, X., Sun, Z.Z., Dong, Q.Q., 2021. The unified pipe-interface element method for simulating the coupled hydro-mechanical grouting process in fractured rock with fracture propagation. Eng. Fract. Mech. 256, 107993. https://doi.org/ 10.1016/j.engfracmech.2021.107993.
- Zeng, Y.J., Chen, Z., Bian, X.B., 2016. Breakthrough in staged fracturing technology for deep shale gas reservoirs in SE Sichuan basin and its implications. Nat. Gas. Ind. 36 (1), 61–67. https://doi.org/10.1016/j.ngib.2016.02.005.

- Zhang, F.S., Zhu, H.Y., Zhou, H.G., 2017. Discrete-element-method/computational-fluid-dynamics coupling simulation of proppant embedment and fracture conductivity after hydraulic fracturing. SPE J. 22 (2), 632–644. https://doi.org/10.2118/185172-PA.
- Zhang, F.S., Damjanac, B., Maxwell, S., 2019. Investigating hydraulic fracturing complexity in naturally fractured rock masses using fully coupled multiscale numerical modeling. Rock Mech. Rock Eng. 52 (12), 5137–5160. https://doi.org/10.1007/s00603-019-01851-3.
- Zhang, F.S., Yin, Z.R., Chen, Z.W., et al., 2020. Fault reactivation and induced seismicity during multistage hydraulic fracturing: microseismic analysis and geomechanical modeling. SPE J. 25 (2), 692–711. https://doi.org/10.2118/199883-PA.
- Zhang, F.S., Huang, L.K., Yang, L., et al., 2022. Numerical investigation on the effect of depletion-induced stress reorientation on infill well hydraulic fracture propagation. Petrol. Sci. 19 (1), 296–308. https://doi.org/10.1016/j.petsci.2021.09.014.
- Zhang, F.S., Dontsov, E., 2018. Modeling hydraulic fracture propagation and proppant transport in a two-layer formation with stress drop. Eng. Fract. Mech. 199, 705–720. https://doi.org/10.1016/j.engfracmech.2018.07.008
- 705–720. https://doi.org/10.1016/j.engfracmech.2018.07.008.
 Zhang, R.X., Hou, B., Han, H.F., et al., 2019. Experimental investigation on fracture morphology in laminated shale formation by hydraulic fracturing. J. Petrol. Sci. Eng. 177, 442–451. https://doi.org/10.1016/j.petrol.2019.02.056.
- Zhang, X., Jeffrey, R.G., 2008. Reinitiation or termination of fluid-driven fractures at frictional bedding interfaces. J. Geophys. Res. Solid Earth 113, B08416. https:// doi.org/10.1029/2007/B005327.

- Zhao, H.F., Chen, M., 2010. Extending behavior of hydraulic fracture when reaching formation interface. J. Petrol. Sci. Eng. 74 (1–2), 26–30. https://doi.org/10.1016/j.petrol.2010.08.003.
- Zhao, H.F., Chen, H., Liu, G.H., et al., 2013. New insight into mechanisms of fracture network generation in shale gas reservoir. J. Petrol. Sci. Eng. 110, 193–198. https://doi.org/10.1016/j.petrol.2013.08.046.
- Zheng, Y.X., He, R., Huang, L.K., et al., 2022. Exploring the effect of engineering parameters on the penetration of hydraulic fractures through bedding planes in different propagation regimes. Comput. Geotech. 146, 104736. https://doi.org/10.1016/j.compgeo.2022.104736.
- Zhou, J., Zhang, L., Pan, Z., et al., 2016. Numerical investigation of fluid-driven near-borehole fracture propagation in laminated reservoir rock using PFC2D. J. Nat. Gas Sci. Eng. 36, 719–733. https://doi.org/10.1016/j.jngse.2016.11.010.
 Zhu, H.Y., Zhang, X.D., Guo, J.C., et al., 2015. Stress field interference of hydraulic
- Zhu, H.Y., Zhang, X.D., Guo, J.C., et al., 2015. Stress field interference of hydraulic fractures in layered formation. Geomechanics and Engineering 5, 645–667. https://doi.org/10.12989/gae.2015.9.5.645.
- Zou, Y.S., Ma, X.F., Zhang, S.C., et al., 2016a. Numerical investigation into the influence of bedding plane on hydraulic fracture network propagation in shale formations. Rock Mech. Rock Eng. 49 (9), 3597–3614. https://doi.org/10.1007/s00603-016-1001-5.
- Zou, Y.S., Zhang, S.C., Zhou, T., et al., 2016b. Experimental investigation into hydraulic fracture network propagation in gas shales using CT scanning technology. Rock Mech. Rock Eng. 49 (1), 33–45. https://doi.org/10.1007/s00603-015-0720-3.